Precision Engineering 33 (2009) 378–386

Contents lists available at ScienceDirect

Precision Engineering

journal homepage: www.elsevier.com/locate/precision

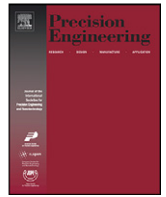

Fundamental investigation of subsurface damage in single crystalline silicon caused by diamond machining

Jiwang Yan[a,*], Tooru Asami[a], Hirofumi Harada[b], Tsunemoto Kuriyagawa[a]

[a] Department of Nanomechanics, School of Engineering, Tohoku University, Aramaki Aoba 6-6-01, Aoba-ku, Sendai 980-8579, Japan
[b] Siltronic Japan Corporation, 3434 Shimata, Hikari, Yamaguchi 743-0063, Japan

ARTICLE INFO

Article history:
Received 30 January 2008
Received in revised form 18 October 2008
Accepted 22 October 2008
Available online 24 November 2008

Keywords:
Single crystal silicon
Nano precision cutting
Ductile machining
Phase transformation
Dislocation
Subsurface damage
High pressure

ABSTRACT

Single crystalline silicon was plunge-cut using diamond tools at a low speed. Cross-sectional transmission electron microscopy and laser micro-Raman spectroscopy were used to examine the subsurface structure of the machined sample. The results showed that the thickness of the machining-induced amorphous layer strongly depends on the tool rake angle and depth of cut, and fluctuates synchronously with surface waviness. Dislocation activity was observed below the amorphous layers in all instances, where the dislocation density depended on the cutting conditions. The machining pressure was estimated from the micro-cutting forces, and a subsurface damage model was proposed by considering the phase transformation and dislocation behavior of silicon under high-pressure conditions.

© 2008 Elsevier Inc. All rights reserved.

1. Introduction

Precision machining of single-crystal silicon has become tremendously important both technologically and economically in microelectronic, micromechanical and optical element manufacturing. As the line widths of the integrated circuits become finer and finer, approaching several tens of nanometers, extremely flat and smooth silicon substrates are required. Therefore, the improvement of the "surface integrity" of silicon has been a focused research topic during the past decade. The topic of "subsurface integrity" has recently gained importance as well. Since all mechanical machining processes involving tool-workpiece contacts inevitably cause subsurface damage, the depth and structure of the near-surface layer will influence the mechanical, optical and electronic performance of silicon products. However, to date, the subsurface damage mechanism of silicon has remained unclear and many aspects related to this issue are still controversial. The lack of literature in this area is primarily due to technological difficulties in precise characterization of the subsurface damage, which is invisible from the surface.

A number of researchers have used cross-sectional transmission electron microscopy (TEM) to observe the subsurface structure of machined silicon wafers. For example, TEM studies on diamond-turned silicon surfaces by Shibata et al. revealed that machining led to the formation of a 150-nm-thick amorphous layer above a 2–3 μm deep crystalline region with dislocation loops [1]. Jeynes et al. showed that a 110-nm-thick amorphous layer was formed above a ∼260-nm-deep dislocated crystalline region during diamond turning [2]. Puttick et al. demonstrated that the total depth of the subsurface damage, including amorphous layers and dislocations, was in the 100–400 nm range for both diamond turned and ground silicon [3]. Zarudi and Zhang investigated the grinding-induced damage to silicon using TEM and energy dispersive spectroscopy (EDS) [4]. A few other studies on machining damage in silicon via X-ray diffraction [5], Raman scattering [6], micro laser Raman [7,8], and a combination of laser Raman and chemical etching [9] have also been reported. However, to date, no systematic study on the relationship between subsurface damage and machining conditions can be found in the literature. For manufacturing engineers, finding the optimum machining conditions that produce minimum subsurface damage in silicon wafers remains a difficult issue.

The objective of the present study is to investigate the subsurface damage mechanism in silicon and to establish its relationship to machining conditions. We used two different methods to characterize subsurface damage: laser micro-Raman spectroscopy and cross-sectional TEM. Laser micro-Raman spectroscopy is a powerful method for materials characterizations. In a previous paper [10], we proposed a method to quantitatively measure the depth of the machining-induced amorphous layer by analyzing the Raman

* Corresponding author. Tel.: +81 22 7956946; fax: +81 22 7957027.
E-mail address: yanjw@pm.mech.tohoku.ac.jp (J. Yan).

0141-6359/$ – see front matter © 2008 Elsevier Inc. All rights reserved.
doi:10.1016/j.precisioneng.2008.10.008

Downloaded from Yan Laboratory, Keio University at http://www.yan.mech.keio.ac.jp. Redistribution is subject to copyright licence from the journal publisher.

intensity data. We found that there was a close correlation between the Raman intensity ratio and the depth of the amorphous layer, which can be used to measure the subsurface damage depth of silicon quickly and in a nondestructive manner.

To prepare the experimental samples, we used the plunge-cutting method. In plunge-cutting, individual cuts are made on pristine single crystalline silicon without preexisting defects. It is different from diamond turning, where due to the cross feeds of the tool, all cuts except the first are made on a subsurface-damaged material and not on the starting crystalline material [8,11]. Also, in plunge cuts, micromachining forces can be measured precisely without the influence of dynamical disturbances. Moreover, thermal effects can be neglected when the cutting speed is low. Furthermore, the tool geometry used for plunge-cutting is well-defined, and a continuous change in depth of cut can be easily achieved in a single cut. The results obtained from plunge-cutting can be used to understand the subsurface damage mechanism in abrasive machining processes, such as grinding, lapping and polishing, where the definition of cutting edge geometry and depth of cut is difficult.

2. Experimental

As shown in Fig. 1, a diamond-cutting tool is subjected to a transverse feed in the x direction while the depth of cut changes continuously in the z direction. In this way, a microgroove with varying depth (schematized in Fig. 2) can be obtained during a single cut. Machining tests were conducted with an ultraprecision lathe (Toyoda AHN-05, JTEKT Corporation, Japan), whose tables have the capability to move under four-axis (XYZB) numerical control at a stepping resolution of 1 nm. Fig. 3 is a photograph of the main section of the machine. A piezoelectric dynamometer (Kistler 9256A) was mounted below the workpiece to measure micro-cutting forces during the cutting tests.

The cutting tool is made of single-crystal diamond and has a nose radius (R_n) of 10 mm. The edge radius R_e was estimated to be around 50 nm by the diamond tool manufacturer using a special scanning electron microscope (SEM) having two electron detectors [12]. The tool rake angle γ was changed from -15° to -60° by adjusting the B-axis rotary table on which the diamond tool was fixed. The relief angle was changed accordingly (from 21° to 66°). Depth of cut d was changed from 0 to 500 nm at a constant cutting speed of 500 mm/min (0.0083 m/s), far lower than that of fly cutting (15–18 m/s) [13] and diamond turning processes. At such a low cutting speed, the effects of cutting heat generation will be insignificant. As lubricant and coolant, the cutting oil Bluebe #LB10 was used in the form of mist jet.

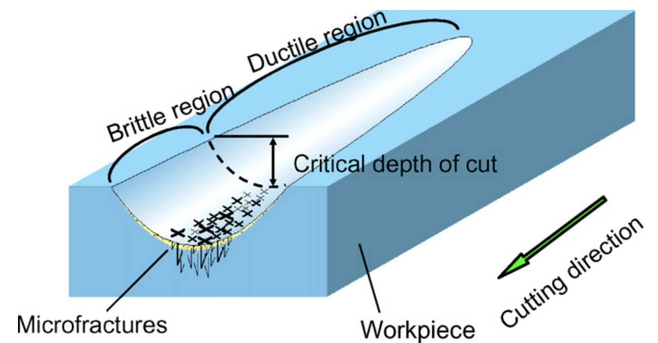

Fig. 2. Schematic model of a microgroove plunge-cut with a round-nosed tool.

As workpiece, an electric-device-grade n-type single-crystal silicon (1 0 0) wafer was machined. The wafer was 150 mm in diameter, 550 μm in thickness and obtained with a chemomechanical polish finish. In this paper, we report results for cutting tests performed along the [1 1 0] direction, which is perpendicular to the orientation flat of the wafer. The effect of crystallographic orientation on the subsurface damage mechanism is another complex issue, which will be reported in detail in a future paper.

The machined samples were first observed by a Nomarski microscope, and then their three-dimensional surface topographies were measured using a white-light interferometer (NewView-5000, Zygo Corporation, USA). A laser micro-Raman spectrometer (NRS-3100, JASCO Corporation, Japan) was used to characterize the material structural changes. The laser wavelength was 532 nm and the output laser power was 10 mW. A 100× objective lens with a numerical aperture (NA) of 0.95 was used so that the focused laser spot size was 1 μm, which enables the laser spot to be directed to any location within the machined microgrooves. To minimize experimental error, all measurements were performed under the same strictly controlled conditions at room temperature.

In order to examine the subsurface structure of machined samples in detail, we also performed cross-sectional TEM (H-9000NAR, Hitachi Ltd., Japan). The TEM samples were cut out from the center of the microgroove bottom and thinned to about 100 nm by the focused ion beam (FIB) technique to enable electron transmission. The acceleration voltage used was 300 kV. To protect from possible damage from the FIB, carbon (C) and tungsten (W) coatings were deposited on the samples.

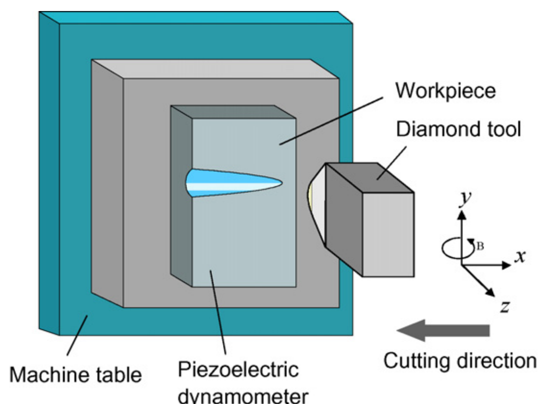

Fig. 1. Schematic of plunge-cutting experiment.

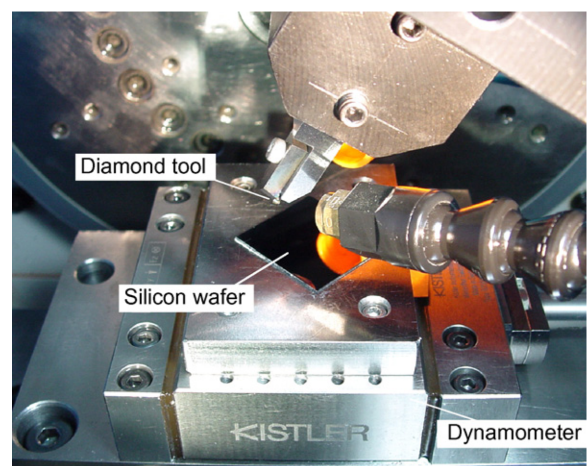

Fig. 3. Photograph of the main section of the experimental setup.

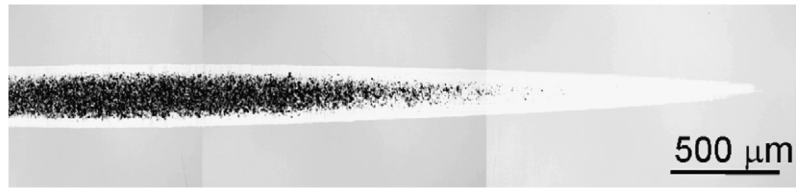

Fig. 4. Micrograph of a plunge-cut microgroove on silicon wafer.

3. Results

3.1. Surface topography

Fig. 4 is a micrograph of a microgroove on the silicon wafer plunge-cut using a −30° rake angle tool. From the right to the left of the figure, as the depth of cut increases, the microgroove is gradually broadened. At a critical depth of cut, microfractures begin to form, and the density of microfractures increases with the depth of cut. It can be seen that the microfractures are concentrated along the center of the groove bottom, while areas near the fringes of the microgroove where the local depth of cut is shallow are smooth. Hence, a clear brittle-ductile transition boundary can be identified on the groove surface.

Fig. 5 shows three-dimensional topographies of the microgroove generated at various depths of cut. In the beginning of the cut (Fig. 5(a)) and the ductile cut at a larger depth (Fig. 5(b)), the groove surface is very smooth without any pileups and visible damage, indicating an excellent geometrical transferability between the diamond tool and silicon. The nanometer-level waviness observed on the groove surface might have been caused by extremely small-amplitude vibrations between the cutting tool and the workpiece. As the depth of cut is further increased, numerous microfractures begin to form on the bottom of the groove while the area near the fringe remains smooth (see Fig. 5(c)).

Next, we measured the critical depth of cut from the cross-sectional profiles of the microgrooves where brittle-ductile transition occurred. Five cuts were made at each tool rake angle and the average critical depths of cut were 109 nm, 146 nm, and 110 nm for the −15°, −30° and −45° tool rake angles, respectively. It should be mentioned that when the tool rake angle was set to −60°, the critical depth of cut showed a large divergence. For a few cuts, significant material swelling occurred on the groove bottom, which made it difficult to measure the critical depth of cut accurately. The swelling was presumably caused by the downward flow and subsequent recovery of the material under highly negative rake angles [14]. The present results indicate that a moderate tool rake angle of around −30° can achieve the best cutting performance in plunge-cut tests, which is slightly different from the results of diamond turning, where the maximum critical depth of cut was achieved around a tool rake angle of −40° [14]. This difference is presumably caused by two factors: (i) since diamond turning involves tool cross-feed, subsequent cuts are actually made on a subsurface-damaged material formed by previous cuts; (ii) the effect of tool relief angle. In previous diamond turning tests, diamond tools of the same relief angles were used.

3.2. Raman spectroscopy

Laser micro-Raman tests were conducted at different points within the ductile-cut microgrooves. Fig. 6(a) shows the Raman spectrum of a sample machined at a depth of cut of 5 nm with the −30° rake angle tool. There is only a sharp peak at 521 cm^{-1}; responses at other Raman shifts are vanishingly weak. This indicates that the structural change in the single crystalline silicon under these conditions is so insignificant that it cannot be detected by the present laser Raman system. Fig. 6(b) is the Raman spectrum of a sample machined at a depth of cut of 120 nm. There are two characteristic peaks in the spectrum: a sharp peak at 521 cm^{-1} and a broadband peak centered at 470 cm^{-1}. This is the typical Raman spectrum for diamond-machined silicon, which demonstrates that a thin layer of silicon has been transformed into the amorphous state (*a*-Si), with the bulk region remaining crystalline (*c*-Si) [8,10].

Fig. 7 shows the variation in the thickness of the *a*-Si layer with depth of cut and tool rake angle in the ductile-cut regions. The thickness of the *a*-Si layer in the figure was calculated from the Raman intensity ratio *r* by the method reported in Ref. [10]. The Raman intensity ratio *r* is defined as

$$r = \frac{I_a}{I_c} \tag{1}$$

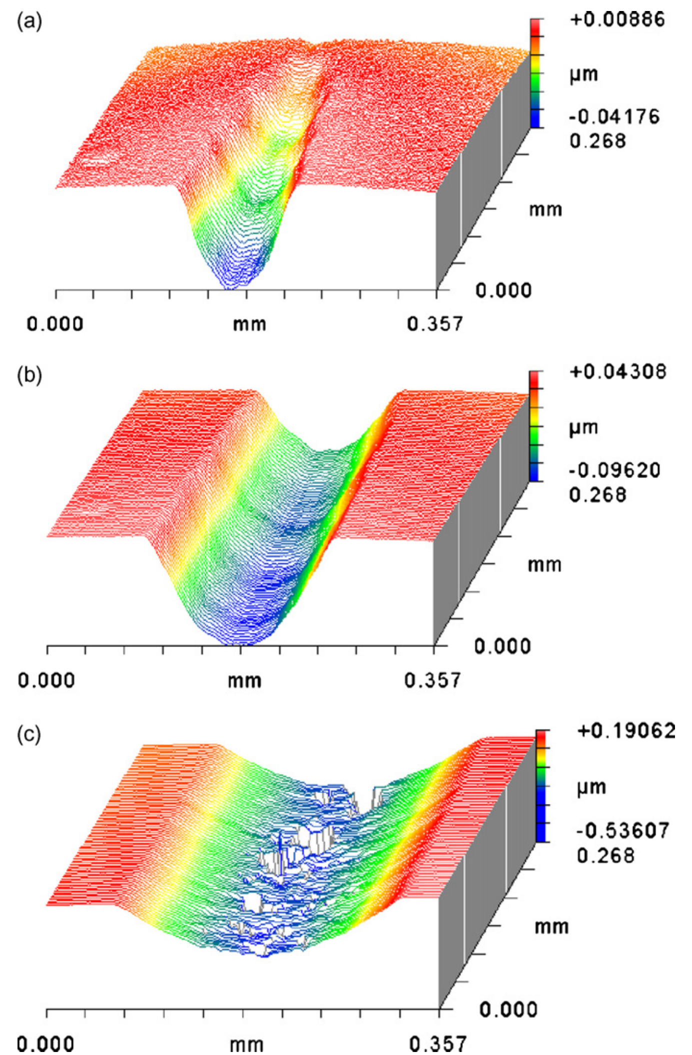

Fig. 5. Three-dimensional topographies of a microgroove plunge-cut at different depths of cut: (a) 0–40 nm, (b) 100–140 nm, (c) 320–360 nm.

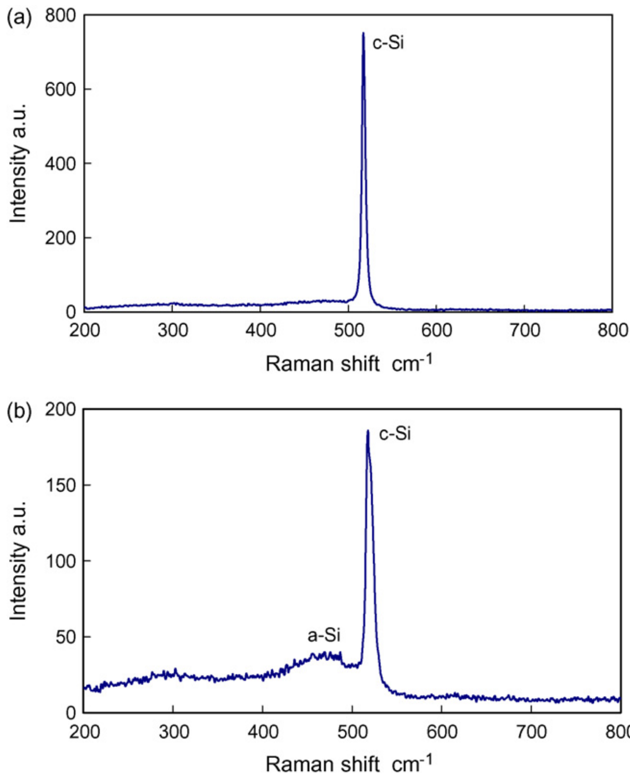

Fig. 6. Raman spectrum of surfaces machined at depths of cut of (a) 10 nm and (b) 140 nm.

where I_a is the total Raman intensity of the amorphous silicon, and I_c is the total Raman intensity of the crystalline silicon. The values of I_a and I_c were obtained by integrating, respectively, the Gauss- and Lorenz-fitted curves of the *a*-Si and *c*-Si peaks in the Raman spectra with respect to the Raman shift. It has been verified that there is a linear relationship between the Raman intensity ratio and the depth of the amorphous layer within an effective measurement range of 10–150 nm [10].

It can be seen that for tool rake angles −15° and −30°, the *a*-Si layer depth increases gradually with the depth of cut at the beginning of the cut (shallow region) and then tends to remain constant as the depth of cut increases further (deep region). A similar trend is observed for the −45° rake angle, but the slope of the *a*-Si layer depth increase at the beginning of the cut is distinctly steeper than those of −15° and −30°. However, when cutting with the −60° rake angle tool, the thickness of amorphous silicon increases in proportion to the depth of cut. As a result, a very thick amorphous layer is formed at large depths of cut.

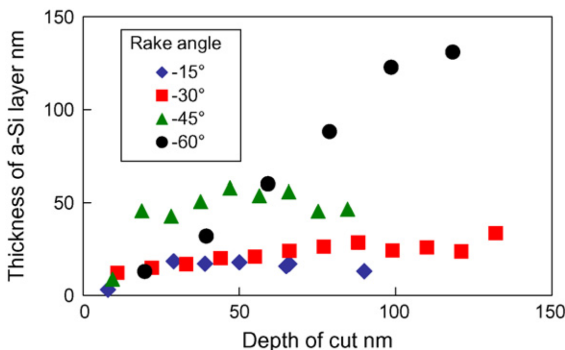

Fig. 7. Variation of the amorphous silicon layer thickness with depth of cut and tool rake angle.

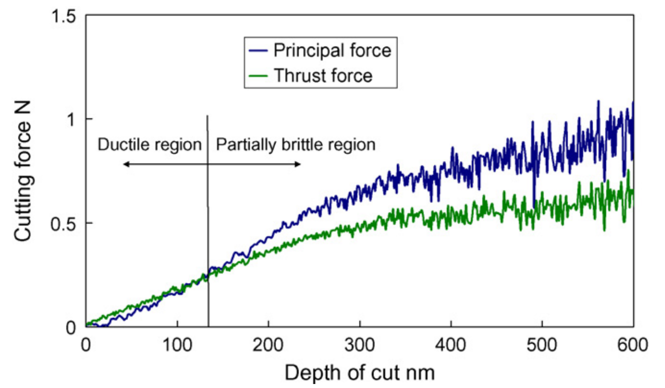

Fig. 8. Variations of the principal and thrust cutting forces during a single plunge cut.

3.3. *Cutting force and machining pressure*

The phase transformation of silicon during machining is presumably related to the high contact pressure between the diamond tool and the workpiece. To examine the contact pressure, we measured the micro-cutting forces during all cuts. As an example, Fig. 8 presents the changes in principal force and thrust force in a single plunge cut with a −30° rake angle tool. During this cut, at a depth of cut of 130 nm, microfractures began to form at the bottom of the groove, thus the machining mode switches into a partially brittle mode. As the depth of cut increases, both the principal force and the thrust force increase, but the slope of the force increase in the partially brittle region is remarkably smaller than that in the ductile region. We also note that in the ductile-cut region, the thrust force is larger than the principal force (depth of cut <120 nm), whereas in the partially brittle region, the principal force becomes predominant (depth of cut >150 nm). Similar phenomena were observed for the other cutting tests.

Next, we estimated the machining pressure, *p*, namely, the average contact pressure between the tool and the workpiece, based on a simplified tool-workpiece contact model (see Fig. 9). The pressure *p* was calculated from the resultant cutting force *F*, which is synthesized from the measured thrust force and principal force, and the effective contact area S_{eq} perpendicular to the force *F*. The detailed calculation procedures of the machining pressure are given in the appendix of this paper. Fig. 10 shows the variation in machining pressure with tool rake angle and depth of cut. In this figure, the data for the cut-in region was omitted because in this region, the calculation results showed significant fluctuation due to the force signal noise. We can see that the machining pressure decreases gradually with increasing depth of cut for each tool rake angle. There was no sudden drop in machining pressure after the microfractures began to form because the fringe regions of the machined microgroove

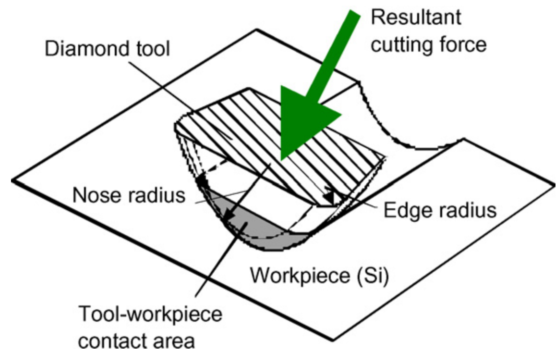

Fig. 9. Simplified model for estimating machining pressure from cutting force.

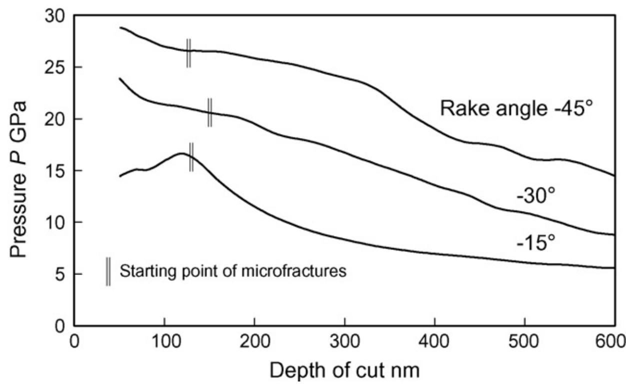

Fig. 10. Variation of machining pressure with tool rake angle and depth of cut.

were still under ductile cut. Fig. 10 also indicates that the higher the negative rake angle is, the higher the pressure is. For all tool rake angles, the machining pressure in the ductile regime is over 10 GPa.

3.4. TEM observation results

Fig. 11 shows a TEM micrograph of the uncut region of the silicon wafer. It can be seen that even at as high a magnification as 500,000, no subsurface defects can be identified. Fig. 12 is a TEM micrograph of the region cut at a depth of 30 nm with a −30° rake angle tool. Clearly, a thin grey layer was generated just beneath the cut surface. This layer, according to selected area diffraction analysis as described in our previous study [10], is amorphous silicon. The average thickness of the layer is approximately 31 nm. However, the thickness of the grey layer is clearly not uniform. A few thick amorphous regions are found at A–A′, B–B′ and C–C′. Near points A, B, and C, the top surface of the *a*-Si layer is higher than the surrounding region, forming small surface peaks, whereas the bottom surface of the *a*-Si layer at points A′, B′, and C′ is lower than neighboring regions, leading to small valleys in the crystalline region. Thus, the thickness of the *a*-Si layer shows synchronic fluctuation with surface waviness. After careful observation, we find that the bottom surface valleys are always on the left side of the surface peaks of the *a*-Si layer, i.e., there is a waviness shift along the cutting direction (leftwards in the figure).

In Fig. 12, in the crystalline region below the amorphous layer, dislocations can be clearly seen. The dislocation density near

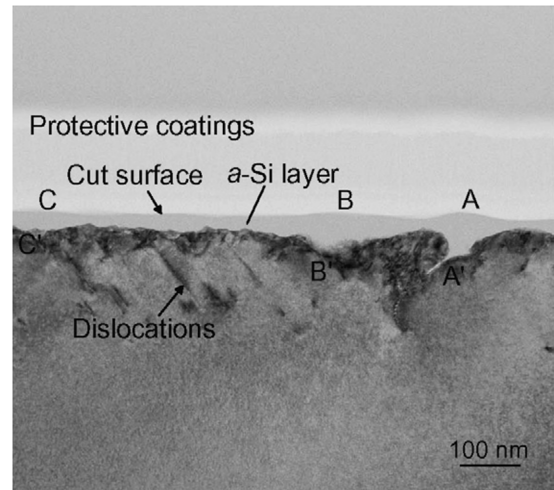

Fig. 12. Cross-sectional TEM micrograph of a region cut at a depth of 30 nm with a −30° rake angle tool.

the amorphous-crystalline interface is higher than that in deeper regions. The thickness of the dislocated layer, namely, the distance from the amorphous-crystalline boundary to the deepest dislocation, is approximately 165 nm. The dislocations are oriented along the [1 1 0] directions (theoretically 54.74° from the cut surface). Also worth noting is the fact that at point A′, there is a sharp protrusion of the amorphous phase into the crystalline region. This protrusion may result from the instable flow of amorphous silicon into a potential microcrack under high pressure. The material around the potential crack exhibits a high dislocation density.

Fig. 13 shows a TEM micrograph of a region cut at a depth of 50 nm with a −45° rake angle tool. Compared to that in Fig. 12, the *a*-Si layer was thicker, and the thickness variation was more significant. However, between points D–D′, E–E′ and F–F′, the synchronic fluctuation of the surface peaks and thickness of the amorphous layer are roughly the same as those in Fig. 12. We also note that, despite the significantly higher dislocation density compared to that in Fig. 12, the thickness of the dislocation layer is almost the same.

Fig. 14 presents TEM micrographs of regions cut with a −60° rake angle tool at depths of 60 nm and 120 nm, respectively [10]. Comparison of (a) and (b) in Fig. 14 reveals that as depth of cut increases, both *a*-Si layer thickness and dislocation density increase.

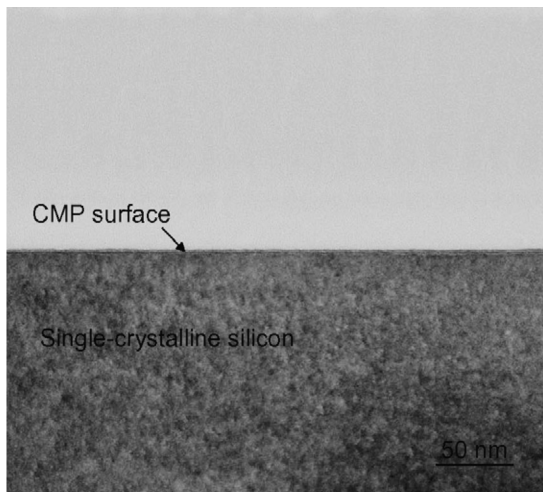

Fig. 11. Cross-sectional TEM micrograph of the uncut region.

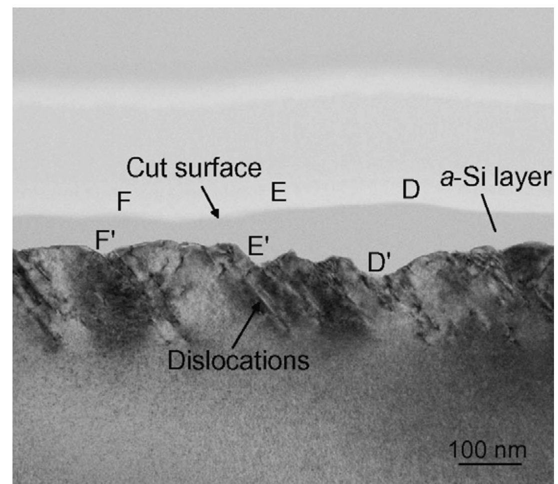

Fig. 13. Cross-sectional TEM micrograph of a region cut at a depth of 50 nm with a −45° rake angle tool.

However, the increase in the dislocation layer thickness is very small. The thickness of the dislocation layer in Fig. 14 is comparable to those in Figs. 12 and 13. Also clearly visible in Fig. 14 is the synchronic fluctuation of the amorphous layer thickness with the surface peaks.

Typical results measured from the TEM micrographs in Figs. 12–14 are summarized in Table 1. It can be seen that the average *a*-Si thicknesses determined by TEM (31 nm for $\gamma = -30^\circ$, $d = 30$ nm; 65 nm for $\gamma = -45^\circ$, $d = 50$ nm; 63 nm for $\gamma = -60^\circ$, $d = 60$ nm; 125 nm for $\gamma = -60^\circ$, $d = 120$ nm) are generally consistent with those obtained by Raman spectroscopy (Fig. 7). Since it is difficult to count the number of dislocations and measure their lengths accurately, we estimated the dislocation density by analyzing the area and contrast level of dislocation regions. First, we measured the total area of dislocations (A_d) by mesh-counting the TEM micrographs, and calculated the dislocation area ratio r by

$$r = \frac{A_d}{A} \quad (2)$$

where A is the area of the region from the amorphous-crystalline interface to the deepest dislocation. Second, the contrast level (l) of the dislocation region in all TEM micrographs was classified into 1, 2, and 3, where a larger number indicated a higher dislocation density for a given dislocation area. Then, we defined a new parameter, namely, relative dislocation density, η:

$$\eta = rl \quad (3)$$

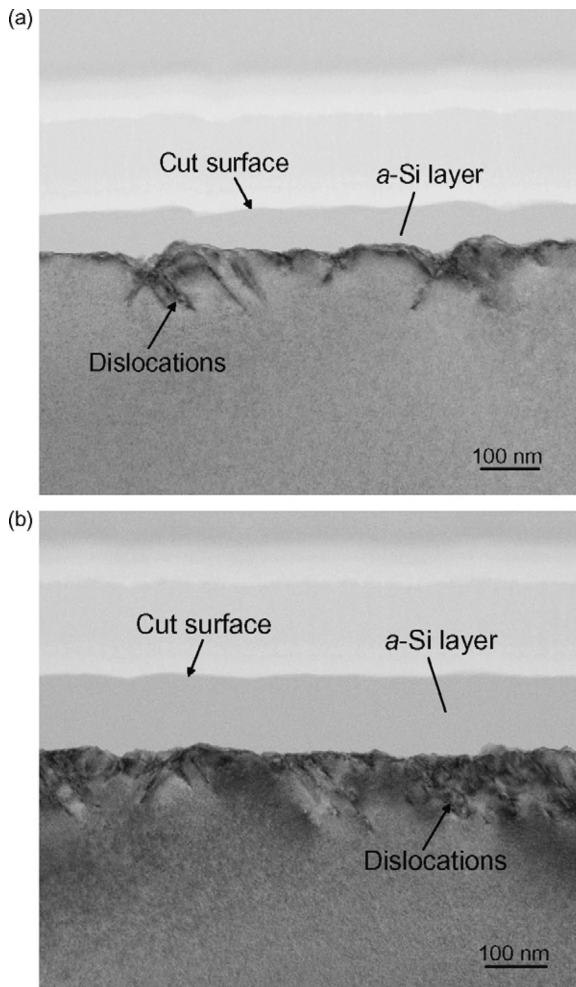

Fig. 14. Cross-sectional TEM micrographs of regions cut with a −60° rake angle tool at depths of (a) 60 nm and (b) 120 nm [10].

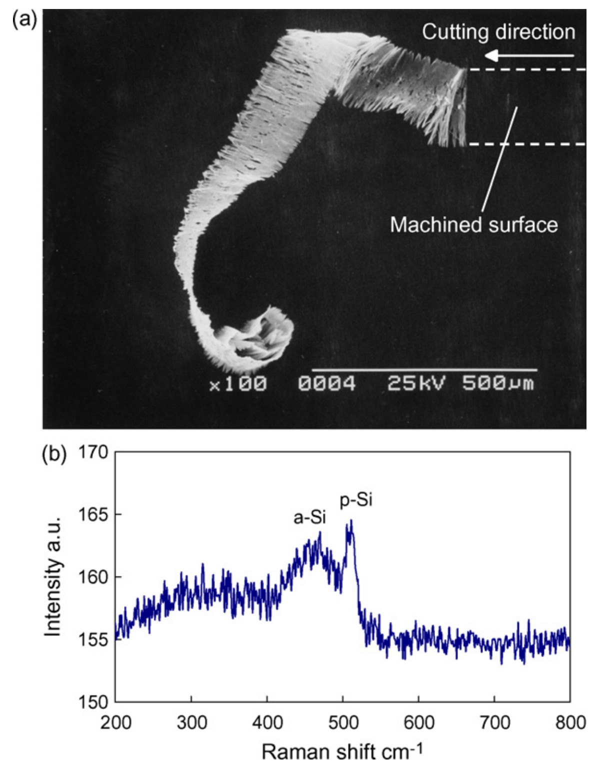

Fig. 15. Observation results of chips: (a) SEM micrograph and (b) Raman spectrum.

Table 1 reveals a general trend: dislocation density increases with depth of cut and changes with tool rake angle. It is worth noting that the −45° rake angle corresponds to the maximum dislocation density, and when the tool rake angle becomes more negative (−60°), the dislocation density decreases. Thus, we can say that at highly negative rake angles, the amorphization of silicon is more significant than the dislocation activity.

3.5. Microstructure of cutting chips

To examine the microstructure of the cutting chips, a few cutting tests were interrupted in the ductile regime by withdrawing the tool from the workpiece. Fig. 15(a) is an SEM micrograph of a chip removed from the workpiece with a −30° rake angle tool in the ductile regime. The chip is long and continuous, and partially curled at its free end. The other end of the chip is still connected to the workpiece. Fig. 15(b) is the Raman spectrum of the chip. These results indicate that the chip is a mixture of amorphous silicon and polycrystalline (microcrystalline) silicon, of which the former is dominant.

4. Discussion

Deformation of the silicon crystal has been a topic of intense research during the past decades. Phase transformation and dislocation mobility are two possible mechanisms for silicon deformation, of which the former is more widely accepted. An abundance of literature has demonstrated that silicon undergoes phase transformation in situations where high hydrostatic pressure exists, like indentation tests [15–27]. It is generally accepted that a structural change from diamond cubic (Si-I) to a metallic state β-Sn (Si-II) occurs under the indenter during loading as a result of the high pressure (10–13 GPa). The material around the indenter would then become ductile enough to sustain plastic flow. Measurements of electrical conductivity during indentation close to the indenter on silicon showed a significant increase in conductivity, from semi-

Table 1
Summary of TEM results.

TEM figure no.	Tool rake angle γ (°)	Depth of cut d (nm)	Min.–max. a-Si thickness (nm)	Average a-Si thickness (nm)	Thickness of dislocation layer (nm)	Dislocation area ratio r (%)	Contrast level l (arb. unit)	Relative dislocation density η (arb. unit)
Fig. 12	−30	30	15–70	31	165	32.7	2	2.1
Fig. 13	−45	50	35–120	65	168	74.1	3	7.1
Fig. 14(a)	−60	60	45–85	63	119	31.3	1	1.0
Fig. 14(b)	−60	120	110–135	125	131	54.9	2	3.5

conducting to highly conducting [15,18], which strongly supports the idea that a transformation into the metallic state occurs underneath the indenter. However, the metallic phase is not stable at low pressure (∼4 GPa). Hence, after the indenter is unloaded, the pressure-induced metallic phase does not transform back into the diamond cubic structure, but instead, changes into an amorphous phase or other metastable phases [18,21–28]. In silicon cutting, the machining pressure in the ductile regime is higher than 10 GPa (see Fig. 10), which is sufficiently high to make silicon undergo phase transformation.

The topic of silicon dislocations is still controversial. Silicon has strong directional covalent bonding with a diamond structure where the predominant slip plane is ⟨1 1 0⟩ {1 1 1}. Pure edge dislocations generally do not form in silicon; rather, pure screw dislocations form with a Burger's vector parallel to the dislocation line. At room temperature, the dislocations are relatively immobile. Dislocation mobility can be induced at higher temperatures and/or high pressures. For example, it was found that under high pressure, dislocation mobility can be activated at a relatively low temperature [17]. Recently, room-temperature dislocation plasticity in silicon has been confirmed by *in situ* nanoindentation in a TEM [29]. In the present study, because the temperature rise is insignificant at a low cutting speed, the dislocations beneath the amorphous layer are presumably due to the high pressure and high shear stress. That is, under the high pressure and high shear stress conditions near the boundary between the phase-transformed region and the crystalline bulk, dislocations are easily initiated. However, the speed of dislocation motion is by far lower than the cutting speed. For instance, the dislocation velocity at 100 °C and 10 GPa is approximately 8.5×10^{-24} m/s, as estimated from the high-temperature experimental data by the interpolation technique (see Table 3 and Eq. (2) in Ref. [30]). Thus, we can say that although dislocations are an important aspect of subsurface damage, they do not contribute directly to the ductile mode removal of silicon.

From the viewpoint of both phase transformation and dislocation, a model of subsurface damage mechanism in ductile machining of silicon is proposed as schematized in Fig. 16. As soon as the tool advances into the material (loading), a phase transformation from diamond cubic structure (Si-I) to metallic phase (Si-II) occurs in the material surrounding the tool tip. This part of the material becomes sufficiently ductile to sustain plastic flow which facilitates ductile-mode material removal. After the tool has passed (unloading), the metallic phase does not transform back into the diamond cubic structure, but rather, changes into an amorphous phase. As a result, the final subsurface damage layer contains an amorphous phase rather than the metallic phase. The metallic phase does not transform to other metastable phases presumably because the unloading speed in cutting is by far higher than that used in the indentation tests. The synchrony between the amorphous layer thickness and surface waviness in Figs. 12–14 may be caused by stick-slips between the diamond tool and the silicon material, which results in unstable changes in machining pressure.

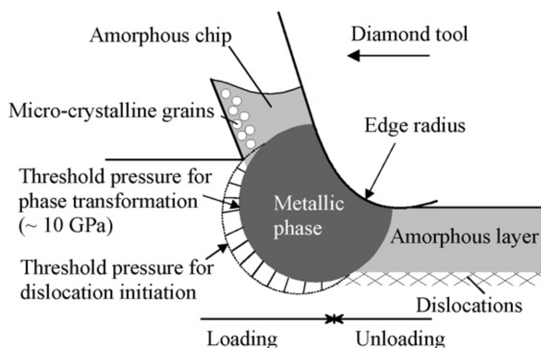

Fig. 16. Schematic model for subsurface damage mechanism in silicon during ductile machining.

In Fig. 16, as the distance from the tool tip increases, the pressure decreases and finally drops below the threshold pressure required for phase transformation (∼10 GPa). However, the pressure may still be high enough to facilitate dislocation initiation in silicon if a sufficiently high shear stress exists. As a result, a dislocation layer is generated beneath the amorphous layer as the tool passes. Under a negative tool rake angle, as depth of cut increases, the shear stresses beneath the tool increase due to the downward material flow, leading to a higher dislocation density. However, the thickness of dislocation layer does not change significantly with machining conditions because the distance between the boundary of threshold pressure for phase transformation and the boundary of threshold pressure for dislocation initiation is not sensitive to cutting conditions.

Phase transformation also occurs in cutting chips. That is, after the chip has been separated from the tool (unloading), a phase transformation from metallic to amorphous takes place in the chip material near the tool, as shown in Fig. 16. However, because the pressure in the material near the free surface of the workpiece is lower than that beneath the tool, the phase transformation in the chip will be incomplete. As a result, the chip becomes partly amorphous and partly crystalline (microcrystalline grains included in the amorphous phase), as seen in Fig. 15. A similar phenomenon has been confirmed in machining germanium by Morris et al. [31].

The present study has experimentally revealed the strong dependence of subsurface structure of machined silicon on tool geometry and machining conditions. As summarized in Table 2, when using a tool with a slightly negative rake angle and a sharp edge, the amorphous layer remains very thin even at a large depth of cut. This is because most of the deformed material will be removed as chip, and the downward flow of material is insignificant. However, when using a highly negative rake angle tool or a blunt tool, except when the depth of cut is extremely small, a very deep subsurface damage layer will be generated. Significant material volume recovery (swelling) will occur after tool pass due to the severe downward flow of the deformed material [14], which is similar to the phenomenon observed in metal cutting [32]. Thus, through proper design of the tool edge geometry (or the abrasive grain size in grinding), it should be possible to optimize the stress field ahead of/beneath the tool (or the grinding wheel), which would not only enable a high ductile material removal rate but also improve the subsurface integrity of silicon wafers. The findings from this study also provide important reference for parameter selection in the

Table 2
Schematic presentation of subsurface structural changes with tool geometry and depth of cut in ductile machining of silicon.

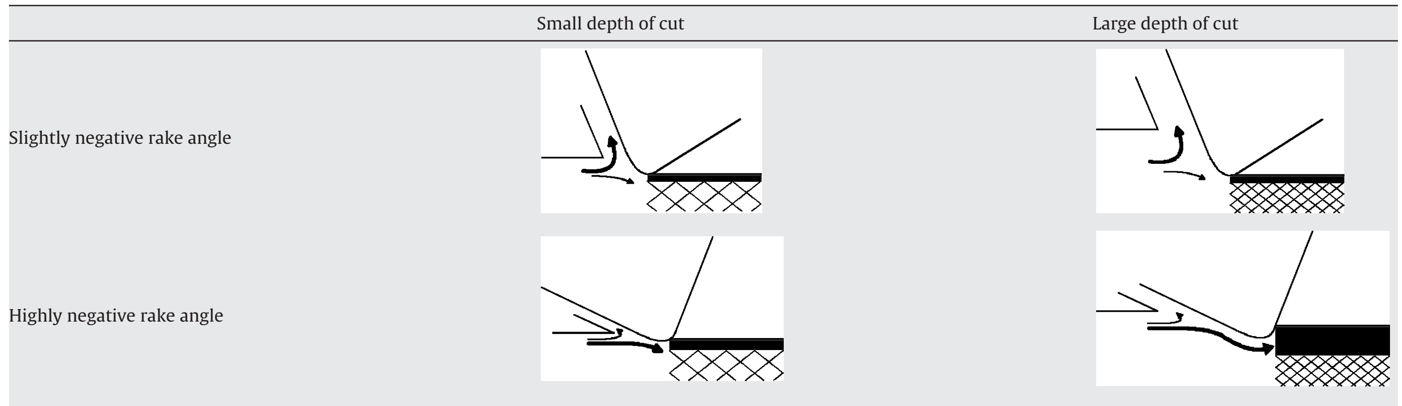

	Small depth of cut	Large depth of cut
Slightly negative rake angle		
Highly negative rake angle		

damage-removing processes, such as chemomechanical polishing and laser irradiation [33].

5. Conclusions

Plunge-cutting tests have been made on single crystalline silicon at various depths using diamond tools with different rake angles. The subsurface structure of silicon after machining was investigated. The main conclusions are as follows:

(1) The machining-induced subsurface damage exhibits two features: amorphization and dislocations. The near-surface layer is transformed into an amorphous phase above a dislocation layer.
(2) At slightly and moderately negative tool rake angles (between -15° and -45°), the thickness of the amorphous layer increases gradually with depth of cut at the beginning of the cut and tends to approach a constant value as depth of cut increases further. At highly negative tool rake angles ($\sim -60^\circ$), the amorphous layer thickness increases in proportion to depth of cut.
(3) The subsurface damage mechanism in silicon is related to machining pressure. The estimated machining pressure (>10 GPa) is sufficiently high to cause phase transformation in silicon. The higher the negative rake angle, the higher the machining pressure.
(4) The thickness of the amorphous layer shows synchronous fluctuation with surface waviness, with a spatial shift along the cutting direction.
(5) The dislocation density depends on depth of cut and tool rake angle, while the dislocation layer thickness is insensitive to changes in machining conditions.
(6) Chips removed from the workpiece during cutting are a mixture of an amorphous phase and a polycrystalline phase.

Acknowledgements

The authors would like to acknowledge the financial support of the Japan Society for the Promotion of Science (JSPS), Grant-in-Aid for Exploratory Research (project no. 20656023), and the Japan New Energy and Industrial Technology Development Organization (NEDO).

Appendix A. Calculation of machining pressure

This appendix will detail the calculation procedure for the machining pressure p, the results of which have been used in Section 3.3. Pressure p can be expressed as

$$p = \frac{F}{S_{eq}} \tag{A.1}$$

where F is the resultant cutting force, which is derived from the experimentally measured thrust force and principal force; S_{eq} is the effective contact area between tool and workpiece, which is the projected area of the actual tool-workpiece contact area in the plane perpendicular to F.

The three-dimensional model of the tool-workpiece contact shown in Fig. 9 can be redrawn into two-dimensional models as schematized in Fig. A.1(a) and (b). Using these models, the effective tool-workpiece contact area S_{eq} can be calculated using the depth of cut d, tool rake angle γ, edge radius R_e and nose radius R_n. In these models, for simplicity, the tool-workpiece friction was not considered. We also neglected the contact between the removed chip and the tool rake face, and the contact between the tool flank face and the machined surface.

In the calculation, the edge radius R_e was set to 50 nm, which is the same as the experimentally estimated value. The calculation was performed by assuming that the depth of cut was larger than

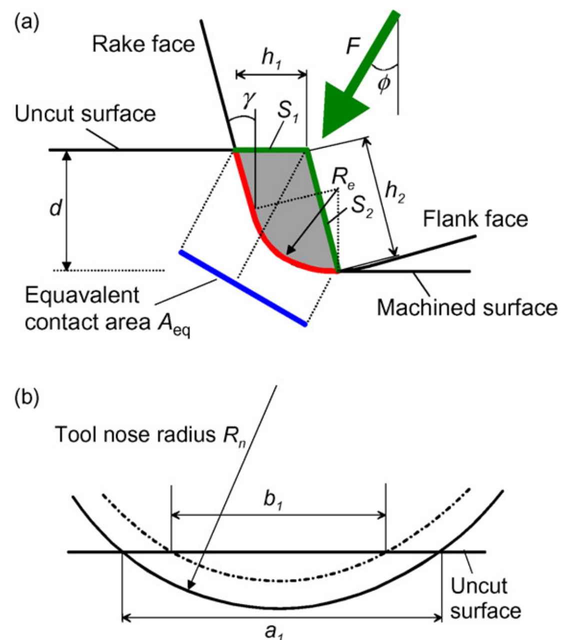

Fig. A.1. Schematic model of the contact geometry between diamond tool and workpiece. (a) View along the cutting direction and (b) view perpendicular to the cutting direction.

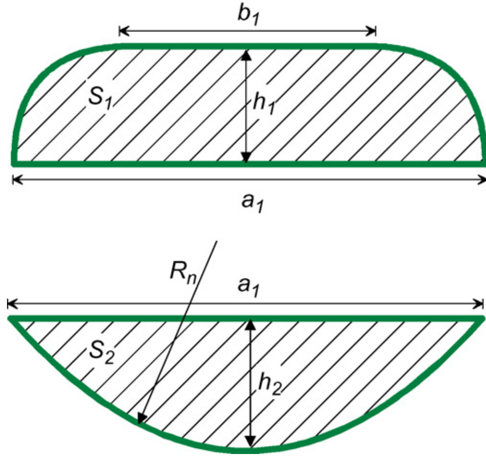

Fig. A.2. Shapes of the two tool cross-sections used to assist the calculation of the effective area of the tool-workpiece contact.

the edge radius, i.e., $d > R_e$. To simplify the calculation of S_{eq}, we first consider two cross-sections of the cutting tool: one intersected by the plane of the uncut surface, whose area is S_1, the other passing through the lowest point in the tool and also parallel to the tool rake face, whose area is S_2. Fig. A.2 shows the shapes of the two cross-sections. The curved sections on the two sides of S_1 are two quarters of an ellipse, and the curve on the lower side of S_2 is equal to the tool nose radius R_n. Thus, the length parameters in Fig. A.2 can be expressed as

$$h_1 = \frac{R_e}{\cos\gamma}(1 - \sin\gamma) \quad (A.2)$$

$$a_1 = \frac{2}{\cos\gamma}\sqrt{2R_n \cos\gamma\, d - d^2} \quad (A.3)$$

$$b_1 = \frac{2}{\cos\gamma}\sqrt{2R_n \cos\gamma(d - h_1\cos\gamma) - (d - h_1\cos\gamma)^2} \quad (A.4)$$

$$h_2 = \frac{d}{\cos\gamma} \quad (A.5)$$

where d is the depth of cut, γ is the tool rake angle, R_e is the edge radius and R_n is the nose radius. So, S_1 and S_2 are given by

$$S_1 = h_1 b_1 + \tfrac{1}{4}\pi h_1(a_1 - b_1) \quad (A.6)$$

$$S_2 = R_n^2 \sin^{-1}\left(\frac{a_1}{2R_n}\right) - \frac{a_1}{2}(R_n - h_2) \quad (A.7)$$

The effective contact area S_{eq} can then be calculated from S_1 and S_2 by the following equation:

$$S_{eq} = S_1 \cos\phi + S_2 \cos\left(\frac{\pi}{2} - \gamma - \phi\right) \quad (A.8)$$

where ϕ is the angle between the resultant force F and the vertical direction, which is calculated from the ratio of the thrust force and principal force. Finally, by substituting S_{eq} into Eq. (A.1), the machining pressure p can be readily obtained.

References

[1] Shibata T, Ono A, Kurihara K, Makino E, Ikeda M. Cross-section transmission electron microscope observations of diamond-turned single-crystal Si surfaces. Appl Phys Lett 1994;65(20):2553–5.
[2] Jeynes C, Puttick KE, Whitmore LC, Gartner K, Gee AE, Millen DK, et al. Laterally resolved crystalline damage in single-point-diamond-turned silicon. Nucl Instrum Meth Phys Res B 1996;118:431–6.
[3] Puttick KE, Whitmore LC, Chao CL, Gee AE. Transmission electron microscopy of nanomachined silicon crystals. Philos Mag A 1994;69(1):91–103.
[4] Zarudi I, Zhang LC. Effect of ultraprecision grinding on the microstructural change in silicon monocrystals. J Mater Process Technol 1998;84: 149–58.
[5] Bismayer U, Brinksmeier E, Güttler B, Seibt H, Menz C. Measurement of subsurface damage in silicon wafers. Prec Eng 1994;16(2):139–44.
[6] Pizani PS, Jasinevicius R, Duduch JG, Porto AJV. Ductile and brittle modes in single-point-diamond-turning of silicon probed by Raman scattering. J Mater Sci Lett 1999;18:1185–7.
[7] Gogotsi Y, Baek C, Kirscht F. Raman microspectroscopy study of processing-induced phase transformations and residual stress in silicon. Semicond Sci Technol 1999;14:936–44.
[8] Yan J. Laser micro-Raman spectroscopy of single-point diamond machined silicon substrates. J Appl Phys 2004;95(4):2094–101.
[9] Chen L, Zhang X, Zhang T, Lin H, Lee S. Micro-Raman spectral analysis of the subsurface damage layer in machined silicon wafers. J Mater Res 2000;15(7):1441–4.
[10] Yan J, Asami T, Kuriyagawa T. Nondestructive measurement of machining-induced amorphous layers in single-crystal silicon by laser micro-Raman spectroscopy. Prec Eng 2008;32:186–95.
[11] Yan J, Takahashi H, Tamaki J, Gai X, Harada H, Patten J. Nanoindentation tests on diamond-machined silicon wafers. Appl Phys Lett 2005;86:181913.
[12] Asai S, Taguchi T, Horio K, Kasai T, Kobayashi A. Measuring and analysis on cutting edge radius of single point diamond tools using newly developed scanning electron microscope (SEM). J Jpn Soc Prec Eng 1990;46(7):145–50.
[13] Yan J, Takahashi H, Tamaki J, Gai X, Kuriyagawa T. Transmission electron microscopic observation of nanoindentations made on ductile-machined silicon wafers. Appl Phys Lett 2005;87:211901.
[14] Yan J, Syoji K, Kuriyagawa T. Effects of cutting edge geometry on brittle-ductile transition in silicon machining. Proceedings of the 9th international conference on precision engineering (ICPE), Osaka, Japan 1999:92–7.
[15] Gridneva IV, Milman YV, Trefilov VI. Phase transition in diamond-structure crystals during hardness measurements. Phys Stat Sol (a) 1972;14: 177–82.
[16] Eremenko VG, Nikitenko VI. Electron microscope investigation of the microplastic deformation mechanism of silicon by indentation. Phys Stat Sol (a) 1972;14:317–30.
[17] Hill MJ, Rowcliffe DJ. Deformation of silicon at low temperatures. J Mater Sci 1974;9:1569–76.
[18] Clarke DR, Kroll MC, Kirchner PD, Cook RF. Amorphization and conductivity of silicon and germanium induced by indentation. Phys Rev Lett 1988;60(21):2156–9.
[19] Pharr GM, Oliver WC, Harding DS. New evidence for a pressure-induced phase transformation during the indentation of silicon. J Mater Res 1991;6(6):1129–30.
[20] Callahan DL, Morris JC. The extent of phase transformation in silicon hardness indentations. J Mater Res 1992;7(7):1614–7.
[21] Kailer A, Gogotsi YG, Nickel KG. Phase transformations of silicon caused by contact loading. J Appl Phys 1997;81(7–1):3057–63.
[22] Bradby JE, Williams JS, Wong-Leung J, Swain MV, Munroe P. Transmission electron microscopy observation of deformation microstructure under spherical indentation in silicon. Appl Phys Lett 2000;77:3749–51.
[23] Zarudi I, Zhang LC. Structure changes in mono-crystalline silicon subjected to indentation—experimental findings. Tribol Int 1999;32:701–12.
[24] Saka H, Shimatani A, Sugamura nad Suprijadi M. Transmission electron microscopy of amorphization and phase transition beneath indents in Si. Philos Mag A 2002;82(10):1971–81.
[25] Zarudi I, Zou J, Zhang LC. Microstructures of phases in indented silicon: a high-resolution characterization. Appl Phys Lett 2003;82(6):874–6.
[26] Jang J, Lance MJ, Wen S, Tsui TY, Pharr GM. Indentation-induced phase transformations in silicon: influences of load, rate and indenter angle on the transformation behavior. Acta Mater 2005;53(6):1759–70.
[27] Yan J, Takahashi H, Gai X, Harada H, Tamaki J, Kuriyagawa T. Load effects on the phase transformation of single-crystal silicon during nanoindentation tests. Mater Sci Eng A 2006;423(1–2):19–23.
[28] Needs RJ, Mujica A. First-principles pseudopotential study of the structural phases of silicon. Phys Rev B 1995;51(15):9652–60.
[29] Minor AM, Lilleodden ET, Jin M, Stach EA, Chrzan DC, Morris JW. Room temperature dislocation plasticity in silicon. Philos Mag 2005;85(2–3): 323–30.
[30] Yonenaga I. Hardness, yield strength, and dislocation velocity in elemental and compound semiconductors. Mater Trans 2005;46:1979–85.
[31] Morris JC, Callahan DL, Kulik J, Patten JA, Scattergood RO. Origins of the ductile regime in single-point diamond turning of semiconductors. J Am Ceram Soc 1995;78(8):2015–20.
[32] Komanduri R. Some aspects of machining with negative rake tools simulating grinding. Int J Mach Tool Des Res 1971;11:223–33.
[33] Yan J, Asami T, Kuriyagawa T. Response of machining-damaged single-crystalline silicon wafers to nanosecond pulsed laser irradiation. Semicond Sci Technol 2007;22:392–5.